

# TriStereoNet: A Trinocular Framework for Multi-baseline Disparity Estimation

Faranak Shamsafar

faranak.shamsafar@uni-tuebingen.de

Andreas Zell

andreas.zell@uni-tuebingen.de

Computer Science Department, University of Tübingen, Germany

## Abstract

Stereo vision is an effective technique for depth estimation with broad applicability in autonomous urban and highway driving. While various deep learning-based approaches have been developed for stereo, the input data from a binocular setup with a fixed baseline are limited. Addressing such a problem, we present an end-to-end network for processing the data from a trinocular setup, which is a combination of a narrow and a wide stereo pair. In this design, two pairs of binocular data with a common reference image are treated with shared weights of the network and a mid-level fusion. We also propose a Guided Addition method for merging the 4D data of the two baselines. Additionally, an iterative sequential self-supervised and supervised learning on real and synthetic datasets is presented, making the training of the trinocular system practical with no need to ground-truth data of the real dataset. Experimental results demonstrate that the trinocular disparity network surpasses the scenario where individual pairs are fed into a similar architecture. Code and dataset: <https://github.com/cogsys-tuebingen/tristereonet>.

## 1. Introduction

While different solutions exist for estimating the depth, stereo matching is the most conforming to various use-cases. Passive recovery of depth maps via stereo has gained attention in the computer vision community for the past three decades. Estimating depth from images can benefit many real-world applications, from which autonomous driving and robot navigation are the most prominent ones. Other active technologies for depth estimation, like Laser Imaging Detection and Ranging (LiDAR) sensors, measure the depth based on the travel time of a light beam emitted by the device. However, in addition to its costly setup, LiDAR yields a sparse depth map, which is also vulnerable to

This work is funded by the Federal Ministry of Education and Research (BMBF) and the Baden-Württemberg Ministry of Science as part of the Excellence Strategy of the German Federal and State Governments.

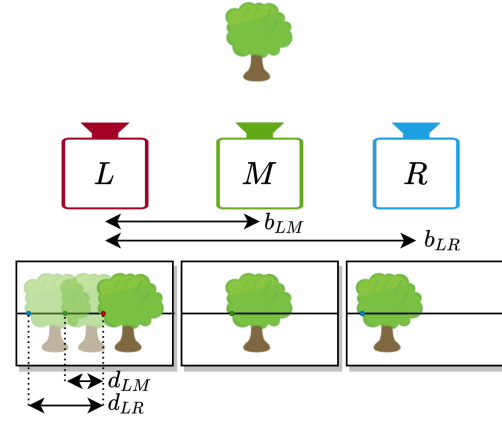


Figure 1. Multi-baseline stereo with three cameras (Left, Middle, Right). Note that disparity (displacement of matching points) is directly dependent on the baseline. The left image is the reference.

weather conditions.

Estimating depth via stereo is computed by finding the disparities between the matching points in the rectified images, through which it gets straightforward to estimate the depth via triangulation. For this, two images are typically taken into account, *i.e.* a binocular setting. There has been an abundance of traditional and deep learning-based strategies to estimate the disparity from a pair of images.

Before deep learning, various hand-engineered features, like Sum of Absolute Difference or Census Transform [36] were used for finding matching points and cost volume computation, followed by a regularization module, such as the renowned Semi Global Matching (SGM) method [15]. On the other hand, deep learning-based methods try to adapt a network for either some steps of stereo vision [28, 37] or the whole pipeline as an end-to-end technique [4, 12, 19, 39]. The latter group has highly boosted the performance of stereo vision in terms of accuracy. The most promising strategies in this regard are the models in which 3D convolutions are utilized on top of a 4D cost volume data [4, 12, 19]. Nevertheless, the applicability of these approaches in real-world scenarios is still an issue due to their bias towards the content of the training images, including the varied object distances to the camera.

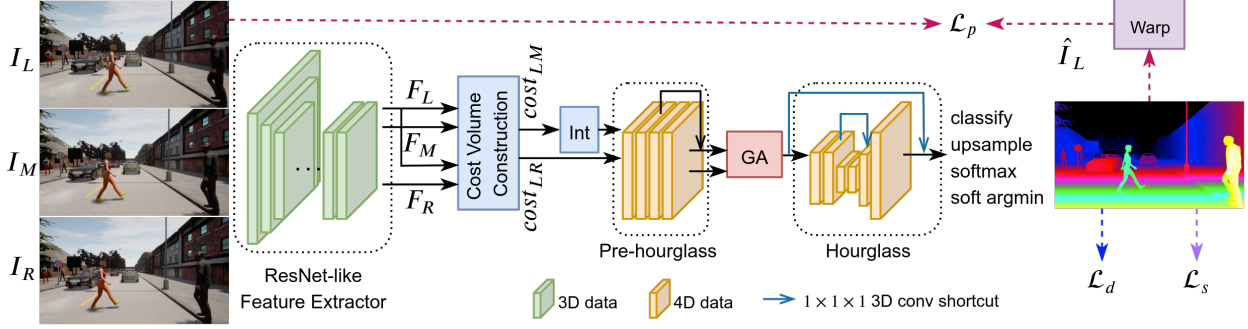


Figure 2. An overview of TriStereoNet architecture. After extracting the feature of the 3-tuple input  $((I_L, I_M, I_R) \rightarrow (F_L, F_M, F_R))$ , cost volumes are computed for the narrow  $((F_L, F_M) \rightarrow cost_{LM})$  and wide  $((F_L, F_R) \rightarrow cost_{LR})$  baselines. “Int” applies the interpolation to stretch  $cost_{LM}$  across the disparity dimension. “GA” or Guided Addition fuses the two streams of data. While  $\mathcal{L}_d$  and  $\mathcal{L}_s$  are used in supervised learning,  $\mathcal{L}_p$  and  $\mathcal{L}_s$  are exploited for self-supervision.

Using multiple images for depth estimation is another alternative, which can bring in more accurate results by providing more visual cues of the scene. Moreover, using more than one fixed baseline is important for many applications, like autonomous driving. This is because while it is essential to get the depth information for close-range distances through a narrow baseline, *e.g.* in low/moderate-speed urban driving settings with more close vehicles or pedestrians, it is undoubtedly vital to infer the accurate depth in speedy driving scenarios in the highways via a wider baseline. Note that depth resolution decreases quadratically with depth in a fixed baseline [9].

In this work, we design a three-view stereo setup (Fig. 1) and propose a deep network (Fig. 2) for estimating the disparity by three inputs. Our work considers two baselines of this trinocular setup with a shared reference image to obtain accurate disparity maps. To the best of our knowledge, the proposed model is the first that processes the multi-baseline trinocular setting in an end-to-end deep learning-based manner. The previous multi-baseline stereo works [16–18] rely on traditional stereo approaches.

The main contributions of this work are summarized as follows: *i)* We design a horizontally-aligned multi-baseline trinocular stereo setup for more accurate depth estimation. Accordingly, an end-to-end deep learning-based model is proposed for processing the 3-tuple input. *ii)* We propose a new layer for merging the disparity-related 4D data for a mid-level fusion. We also investigate other levels and methods of fusion. *iii)* An iterative sequential self-supervised and supervised learning scheme is proposed to make the design practical to new real-world scenarios with no disparity annotations available. *iv)* We build a synthetic dataset for the trinocular design together with the ground-truth information, which is publicly available.

## 2. Related Work

**Classical Stereo Vision.** Classical algorithms for stereo vision can mainly be divided into three modules: match-

ing cost computation, cost regularization, and disparity optimization. For cost regularization, local approaches calculate disparities based on the neighboring pixels [5, 25] with the drawback of the sensitivity to occlusions and uniform texture. Global methods look globally to the disparity changes for higher accuracy owing to the utilization of non-local constraints. These estimations, though, lead to higher computational complexity. Semi-global approaches examine both locally to predict better disparities for small regions and also globally to estimate based on the overall content of the images [15]. Later on, the classical work mostly focused on improving the semi-global estimations in terms of accuracy and speed [10, 24].

**Deep Learning-based Stereo.** With the rise of deep learning, stereo matching continued to be reformed by these modern techniques. Following the general paradigm for stereo reconstruction, deep models can be divided into two categories: the methods that formulate one or some of the steps with a deep learning framework [2, 28, 37], and the approaches that transfer the full process in an end-to-end scheme [4, 12, 19, 21, 29, 39]. Following the recent research, our model is also an end-to-end one, processing a 3-tuple sample.

**Multi-view Stereo.** Depth reconstruction can be conducted in a multi-view setting as well. The advantage of this strategy is the improved robustness, *e.g.* to occlusion or surface texture. Since multi-view stereo is usually designed to deal with a large number of viewpoints, these algorithms are developed differently compared to the classical two-view stereo vision techniques [8]. As an example, a related dataset is DTU [1] consisting of 49 or 64 captured images per scene. More importantly, in multi-view methods, the images are captured at unconstrained camera poses, restricting the possibility of fusing the information from different pairs of images. In our multi-view design, we have an array of axis-aligned cameras, in which the matching pixels locate at the same horizontal line. As a result, the fusion of the stereo pairs is achievable.

**Multi-baseline Stereo.** This concept was initially investigated back in 1993 [26] to benefit from narrow and wide baselines. In [26], the fusion was applied after computing the Sum of Squared Distances (SSD) of images. More recently, authors in [17, 18] extended the standard two-view stereo to a three-view setup by adding a camera on top of the left one. This L-shape configuration creates a vertical and a horizontal baseline. In these works, classical stereo methods, *i.e.* Census Transform and SGM, were utilized with disparity-level and cost volume-level fusion. An FPGA-based multi-baseline stereo system with four cameras was developed in [16] via Census Transform and with no regularization like SGM. The authors showed that their setup is better in recovering fine structures than a binocular setup with SGM. From this viewpoint, we develop a multi-baseline stereo in a full deep learning-based method.

### 3. Methodology

#### 3.1. Motivation

Two-view stereo is a low-cost strategy with dense disparity prediction and higher depth range and resolution than LiDAR-based and monocular depth estimation techniques. However, depending on the operating environment, it suffers from limitations coming from the fixed baseline. In standard stereo, depth resolution drops quadratically with depth [9], making the narrow baseline suitable for closer objects and the wide baseline more fitting for far range. Our motivation for using three cameras for stereo is to leverage both the narrow and the wide baselines for accurate depth estimation. Additionally, in such a setup, the visual data of closer objects that are missed in the field of view of the wider baseline can be recovered by the narrow one. This formulation is particularly necessary for driving scenarios where diversified near- and far-range objects appear.

#### 3.2. Trinocular Stereo Setup

The schematic of our multi-baseline trinocular setup with horizontally-aligned cameras is illustrated in Fig. 1. As identical cameras are located with known and constrained displacement in parallel, not only can stereo matching be obtained between different camera pairs, but we can also fuse these data for accurate and robust prediction. In our formulation, we consider two left-middle ( $b_{LM}/b_{narrow}$ ) and left-right ( $b_{LR}/b_{wide}$ ) baselines with the left image as reference. Note that it is possible to consider other stereo pairs or other reference images. Still, as we evaluate our method in driving scenarios, we fuse the information from the driver’s viewpoint (for the right-hand traffic).

Theoretically, the disparities (displacements) between the matching points in left-middle and left-right pairs depend on the baselines. That is, given  $b_{LR} = r \cdot b_{LM}$ , then  $d_{LR} = r \cdot d_{LM}$ , with  $d$  as the notation for disparity. This

can be proved via triangulation for a fixed object.

In this system, both the LM and LR pairs contribute to disparity estimation. More importantly, their fusion provides more constraints to the problem by needing to satisfy  $d_{LR} = r \cdot d_{LM}$ . Hence, this setup benefits from the wide baseline for more accurate estimation of distant objects and the narrow baseline for depth estimation of closer objects. Note that close objects may be missed in the joint field of view of the cameras with a wide baseline.

#### 3.3. Network Structure

The TriStereoNet architecture is depicted in Fig. 2. We use GwcNet [12] as our model backbone, which was originally proposed for standard binocular stereo. The network is coarsely divided into four main modules: feature extraction, cost volume construction, pre-hourglass ( $4 \times 3D$  convolutions), and 3D convolutional hourglass as encoder-decoder. We suffice the encoder-decoder to a single hourglass architecture for efficiency.

In our formulation for three views, the ResNet-like feature extraction [4, 12] is shared for the three input images ( $I_L, I_M, I_R$ ). For an input image of size  $3 \times H \times W$ , the size of each feature data ( $F_L, F_M, F_R$ ) is  $320 \times H/4 \times W/4$ . After computing the three feature data for the 3-tuple sample, two cost volumes are computed by group-wise correlation [12] (with number of groups as 40) for the left-middle pair ( $cost_{LM}$ ) and the left-right pair ( $cost_{LR}$ ), outputting two 4D cost data of size  $f \times d_{max} \times H/4 \times W/4$  ( $= 40 \times 48 \times H/4 \times W/4$ ). Note that  $d_{max} = 48$  is the maximum disparity range, which is assumed to be 192 for the original input image size.

**Aligning the Cost Volumes.** One notable point is that the baselines of the left-middle and left-right pairs are different. As a result, the disparity range of the two cost volumes should be aligned for fusion. Accordingly, we need to consider  $cost_{LM}(f, d/r, i, j)$  to align the disparity values with  $cost_{LR}(f, d, i, j)$ . Here,  $i, j$  stand for spatial dimension and  $f$  for feature dimension of the 4D cost data. In our setup, the ratio between the baselines is  $r = 2$ . To compute  $cost_{LM}(f, d/r, i, j)$  at non-integer values of the disparity dimension, we need to interpolate the values across the corresponding dimension. To this end, we utilize natural cubic splines with a function as eq. 1 for each sub-interval  $[x_{j-1}, x_j]$  ( $j = 2, 3, \dots, n$ ). For more details on how the related coefficients can be computed, we refer the reader to [22].

$$S_j(x) = a_j + b_j(x - x_j) + c_j(x - x_j)^2 + d_j(x - x_j)^3 \quad (1)$$

**Fusion of Wide- & Narrow-Baseline Data.** An important assumption for this fusion is that all three images are rectified. At this stage, the main questions are *where* and *how* to apply the fusion of the narrow- and wide-baseline data. For this, we propose a *Guided Addition* (GA) module

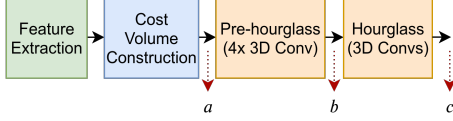


Figure 3. Different levels for merging the narrow- and wide-baseline data: after cost volume (a), after pre-hourglass (b), and after hourglass (c).

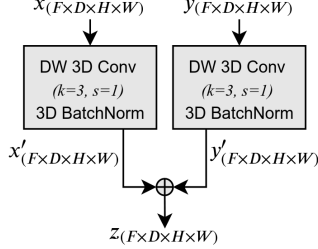


Figure 4. The proposed Guided Addition (GA) layer to merge two 4D data.  $F$ ,  $D$ ,  $H$ - $W$  denote the feature, disparity, and spatial dimensions, respectively.

for merging two streams of the 4D disparity data *after pre-hourglass*. Note that in this architecture, there are mainly three levels for fusion (Fig. 3): *i*) after cost volume computation, *ii*) after pre-hourglass, and *iii*) after hourglass. If data after cost volume computation ( $cost_{LM}$ ,  $cost_{LR}$ ) are processed with a few more convolutions, *i.e.* with pre-hourglass module, their aggregation obtains higher accuracy. Fusion after hourglass also outperforms direct fusion of the cost volumes; however, the complexity increases as the network operates two 4D data (instead of one) in the hourglass with all heavy 3D convolutions.

Figure 4 shows our proposed Guided Addition module for fusing the 4D data. After applying depth-wise 3D convolution across the feature dimension and 3D batch normalization, this layer merges the data by addition. The data size is retained with kernel size as 3, stride as 1, and the same number of channels (features).

We investigated other manners of fusion in cost volume fusion, *i.e.* addition, average, concatenation, maximization and top feature selection. The last method gets the largest elements from the two data across their feature dimension. Also, we examined average and top feature selection for pre-hourglass and hourglass fusion. However, with regard to accuracy and efficiently, we adopted Guided Addition after pre-hourglass for fusion, *i.e.*  $pre\_hg_{ga}$  (c.f. Table 3). We also observed that fusion by addition and average in cost level, and top feature selection in pre-hourglass and hourglass levels do not outperform the single wide baseline (LR), indicating the impact of the appropriate fusion method.

At last, the disparity probabilities are calculated by applying a softmax function at the disparity dimension and using the soft argmin as eq. 2 [19], the final disparity is estimated.  $k$  and  $p_k$  denote a possible disparity level and the

corresponding probability.

$$\hat{d} = \sum_{k=0}^{D_{max}-1} kp_k \quad (2)$$

### 3.4. Learning Mechanism

**Supervised Learning.** By building a trinocular synthetic dataset with ground-truth information, we can apply supervised learning via a loss function between the estimated and the ground-truth disparity maps. To this end, we employ Huber loss as eq. 3, with  $d$  and  $\hat{d}$  as the ground-truth and estimated disparity maps, and  $n$  as the number of image pixels.  $\delta$  is the threshold for the scaled L1 and L2 loss. We will show that the value of  $\delta$  affects the performance. In previous works on disparity estimation [4, 7, 12, 30, 39], smooth L1 loss is used for this goal.

$$\mathcal{L}_d(d, \hat{d}) = \frac{1}{n} \sum_i \begin{cases} 0.5(d_i - \hat{d}_i)^2, & \text{if } |d_i - \hat{d}_i| < \delta \\ \delta \times (|d_i - \hat{d}_i| - 0.5 \times \delta), & \text{otherwise} \end{cases} \quad (3)$$

**Self-supervised Learning.** To demonstrate the performance of TriStereoNet on real-world data and since providing the ground-truth labels for a real dataset is costly, unsupervised learning via a self-supervision loss is utilized. In particular, we consider photometric loss and disparity smoothness loss. To be more precise, we reconstruct the reference image via warping the target one using the estimated disparity. We then use a combination of SSIM [32] and L1 loss as in [11] (eq. 4) to measure image discrepancy between the reconstructed and the original image.

$$\mathcal{L}_p(I, \hat{I}) = \frac{1}{n} \sum_i \alpha \frac{1 - \text{SSIM}(\mathbf{I}, \hat{\mathbf{I}})}{2} + (1 - \alpha) \|\mathbf{I} - \hat{\mathbf{I}}\| \quad (4)$$

$\hat{I}$  is the reconstructed image. We set  $\alpha = 0.85$  and use a SSIM with a  $3 \times 3$  block filter. The reconstructed image is computed according to the disparity map and the baseline. We consider two photometric losses corresponding to the reconstructed left image as eq. 5 and will show that  $\hat{I}_L^R$  outperforms  $\hat{I}_L^M$ . Note that for warping the middle image to reconstruct the left image, we need to use  $\hat{d}/r$  because of  $d_{LR} = r \cdot d_{LM}$ .

$$\hat{I}_L^M = \text{WARP}(I_M, \hat{d}/r), \quad \hat{I}_L^R = \text{WARP}(I_R, \hat{d}) \quad (5)$$

For disparity smoothness loss, we adopt the edge-aware smoothness loss in [13] (eq. 6) to encourage the disparity to be locally smooth. This is an L1 loss on the disparity gradients weighted by image gradients.

$$\mathcal{L}_s(\hat{d}, I_L) = \frac{1}{n} \sum_i \left| \partial_x \hat{d} \right| e^{-\|\partial_x I_L\|} + \left| \partial_y \hat{d} \right| e^{-\|\partial_y I_L\|} \quad (6)$$

**Final Loss.** The final loss is as follows:

$$\mathcal{L} = \lambda_d \cdot \mathcal{L}_d + \lambda_p \cdot \mathcal{L}_p + \lambda_s \cdot \mathcal{L}_s, \quad (7)$$

where  $(\lambda_d, \lambda_p, \lambda_s)$  are loss coefficients. Empirically, the coefficients are set as  $(1.0, 1.0, 0.01)$ . We formulate this loss as a hybrid supervised and self-supervised training. That is, when training on the synthetic dataset, the photometric loss is ignored, *i.e.*  $\lambda_p = 0$ , and when the real dataset is used,  $\lambda_d = 0$ .

**Iterative Sequential Learning Scheme.** Here, we propose a training approach, which is highly efficient with no need for the ground-truth disparity map of the real dataset. First, we initialize the training by self-supervised learning on the real dataset with  $\mathcal{L}_s$  and  $\mathcal{L}_p$  loss functions. Then, moving on with the synthetic dataset, we employ  $\mathcal{L}_s$  and  $\mathcal{L}_d$  losses for supervised learning. This way, we iteratively optimize the network with self-supervised and supervised learning on the real and synthetic datasets, respectively.

The advantage of this technique is three-fold: Firstly, we can efficiently train on the real-world data where no ground-truth is available. Secondly, the supervision provided via the synthetic dataset assists the network in learning fine details as considering only image reconstruction loss ( $\mathcal{L}_p$ ) presents a coarse matching. Finally, self-supervision with no ground-truth helps the network learn the underlying principles of the trinocular setup, hindering the model from overfitting to the ground-truth labels.

## 4. Experiments and Discussion

**Synthetic Dataset.** We generated a synthetic dataset using CARLA [6], consisting of RGB images of three cameras on an axis such that the middle camera is centered in the left-right baseline (38.6 cm). This dataset spans various features provided in CARLA, *i.e.* weather condition, day time, traffic, number of people, and location. Out of the built 25 configurations, the dataset includes 9649/2413 training/test samples. These images with a resolution of  $720 \times 1280$  are rectified, and stereo matching can be performed using any pair of viewpoints. Based on the proposed model and assuming the left image as the shared reference, we only use the left-middle and left-right pairs. Figure 5 shows a 3-tuple sample of this dataset embedded with horizontal lines.

**Real Dataset.** For the real dataset, we consider the trinocular set of images collected by [14, 27]. This dataset is a collection of tricamera stereo sequences with eight sets as Harbour bridge, Barriers, Dusk, Queen street, People, Midday, Night and Wiper. We ignore the Dusk and Night sets for their too bright/dark illumination. The images are in 10-bit gray-scale with a resolution of  $480 \times 640$ . Similar to our CARLA dataset, each 3-tuple sample satisfies the standard epipolar geometry (Fig. 5). From all the samples, we have split the dataset

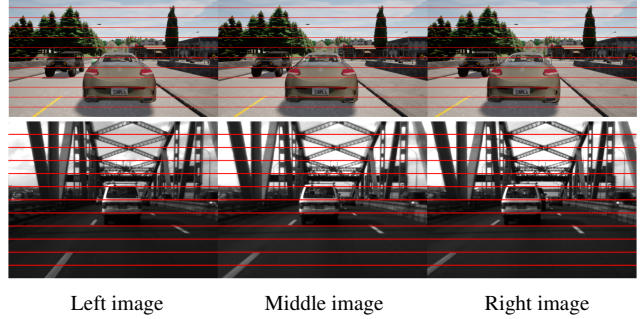


Figure 5. *Top*: Our synthetic trinocular dataset generated by CARLA. *Bottom*: The real trinocular dataset collected by [14, 27]. As seen through the horizontal lines, the 3-tuple samples in both the real and synthetic datasets are rectified.

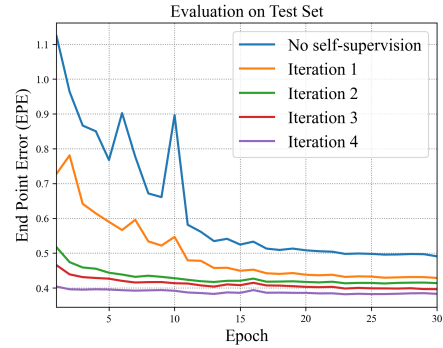


Figure 6. EPE metric on the test set of CARLA dataset when trained from scratch (no self-supervision by the real dataset) and in sequential learning with the self-supervision.

into 1920/480 training/test samples. This dataset does not include ground-truth disparity maps.

**Evaluation Metrics.** We evaluate the performance of TriStereoNet in terms of, *i*) EPE or average End-Point-Error: the mean of absolute error among the valid pixels, *ii*) D1: the percentage of pixels whose estimation error is  $\geq 3px$  or  $\geq 5\%$  of the ground-truth disparity, *iii*) px-1: the portion of pixels for which absolute error is  $\geq 1px$ , *iv*) MRE or Mean Relative Error [31]: the mean of absolute error among the valid pixels divided by the ground-truth disparity, *v*) px-re-1: we define this metric as the percentage of pixels for which MRE is  $\geq 1$ . This metric is actually the average BM-PRE defined in [3], which integrates the benefits of px-1 and MRE. Both MRE and px-re-1 consider depth (and not disparity) error.

In recent works for stereo matching, only EPE and D1 measures are evaluated. We believe considering MRE and px-re-1 metrics are equally important as they better represent the actual estimation error in terms for *depth* (and not disparity), which is the ultimate goal of stereo matching. Note that EPE, D1, and px-1 are incompetent in yielding higher error values for larger triangulation errors [31].

**Implementation Details.** For training, random crops of  $256 \times 512$  are used for both of the datasets. Testing is evaluated on crops of  $512 \times 960$  of the synthetic images.

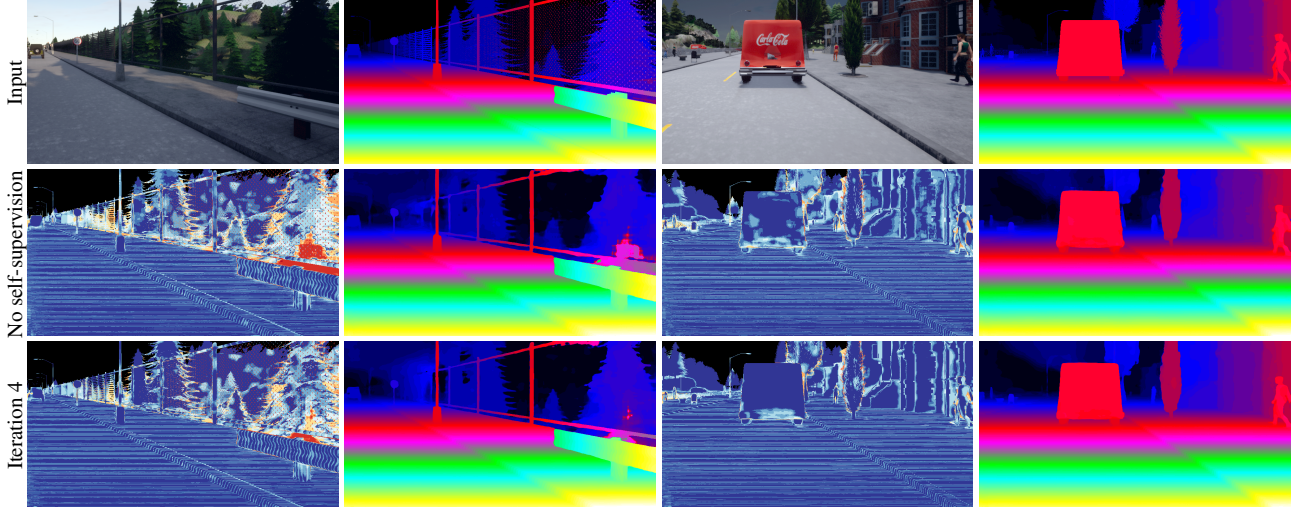


Figure 7. Disparity maps on the test set of the synthetic dataset. In the error maps, warmer colors indicate higher error values. We can see how the proposed sequential learning after 4 iterations outperforms the vanilla training with no self-supervision.

iteration	EPE(px)	D1(%)	px-1(%)	MRE	px-re-1(%)
1	0.43	1.76	5.60	0.045	0.55
2	0.41	1.65	5.29	0.042	0.50
3	0.40	1.57	5.09	0.040	0.48
4	<b>0.38</b>	<b>1.49</b>	<b>4.86</b>	<b>0.038</b>	<b>0.44</b>

Table 1. Performance evaluation on trinocular CARLA dataset. Each iteration consists of sequential self-supervised and supervised training using the real and synthetic datasets. For all metrics, the lower, the better.

Method	EPE(px) ↓	D1(%) ↓	MACs(G) ↓	Params(M) ↓
PSMNet [4]	0.88	2.00	256.66	5.22
GA-Ne-deep [39]	0.63	1.61	670.25	6.58
GA-Net-11 [39]	0.67	1.92	383.42	4.48
GwcNet-gc [12]	0.63	1.55	260.49	6.82
GwcNet-g [12]	<b>0.62</b>	<b>1.49</b>	246.27	6.43
TriStereoNet	0.64	1.71	<b>228.30</b>	<b>4.21</b>

Table 2. Error metrics on the KITTI 2015 validation set and the computational complexity. For TriStereoNet, we assume the middle image is missed and is replaced by the right image. For computing the complexity in terms of MACs, the input resolution is  $256 \times 512$ .

With a batch size of 8, we trained our model on four Nvidia GeForce GTX 1080Ti. For the synthetic dataset, the learning rate starts from 0.001 and is downscaled by a factor of 2 after epochs 10, 12, 14, 16 (in 30 epochs) with Adam optimizer [20]. As for the real dataset, we train the model for 60 epochs with a learning rate downscaled by 2 after epochs 40, 50. We also set  $\delta = 0.25$  for the Huber loss.

**Quantitative and Qualitative Results.** The evaluation on the synthetic dataset is presented in Table 1. We applied four iterations for iterative sequential learning. Namely, each iteration starts by learning on the real dataset (via self-supervision) and then on the synthetic dataset (via supervised training).

From the first iteration to the 4th round, performance im-

proves by approximately 12%, 15%, 13%, 16%, 20% reduction in EPE, D1, px-1, MRE, and px-re-1 measures, respectively. This gain decreases after the 4th iteration. In Fig. 6, we can see the evaluation based on EPE for different iterations of the sequential training. Note that although the learning converges to a reasonable degree in each case, restarting the learning by self-supervision on the real dataset enhances the supervised training on the synthetic dataset. Also, note how this learning mechanism surpasses the vanilla training, *i.e.* from scratch with no self-supervision.

Figure 7 depicts some qualitative results together with the error maps on the synthetic dataset. It is clear that the mechanism of iterative sequential training enhances the estimations. The performance on the real dataset with their 3D reprojections are presented in Fig. 8. Note that this dataset does not have ground-truth information. Besides, these images are challenging as they are different from the synthetic dataset, except they are both driving scenarios.

#### 4.1. Binocular Deployment

We evaluate how TriStereoNet performs on the binocular dataset in case of missing the viewpoint of the middle camera. For this, we assume the right image works as the middle one as well, and finetune the network on 159/40 training/validation split from the KITTI 2015 dataset [23]. The evaluation results are tabulated in Table. 2, including the error rates and the computational complexity in terms of number of operations (MAC) and parameters. We can see that TriStereoNet is capable of estimating the disparity in binocular setup as well, with comparable accuracy and yet with less complexity than binocular models. Notably, it surpasses GA-Net-11 with 40% fewer GigaMACs and is competitive with GA-Net-deep with 66%/36% fewer operations/parameters. We believe the reason lies in multi-view

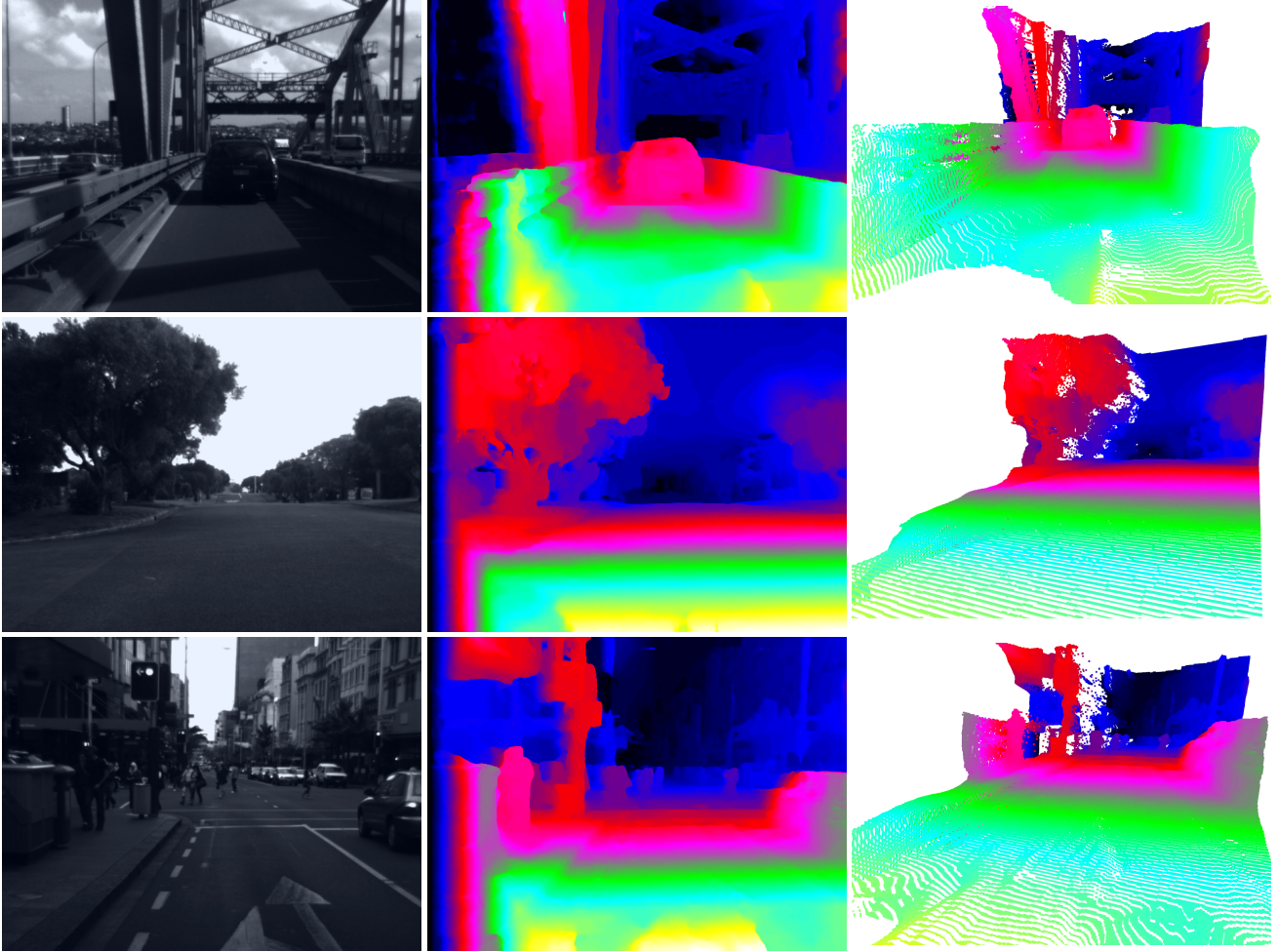


Figure 8. Qualitative results of disparity estimation on the real dataset. Note that this dataset with gray-scale images does not have ground-truth information. The images are challenging due to different illumination from the synthetic data. In particular, the only similarity with the synthetic dataset is “being recorded in a driving scenario”.

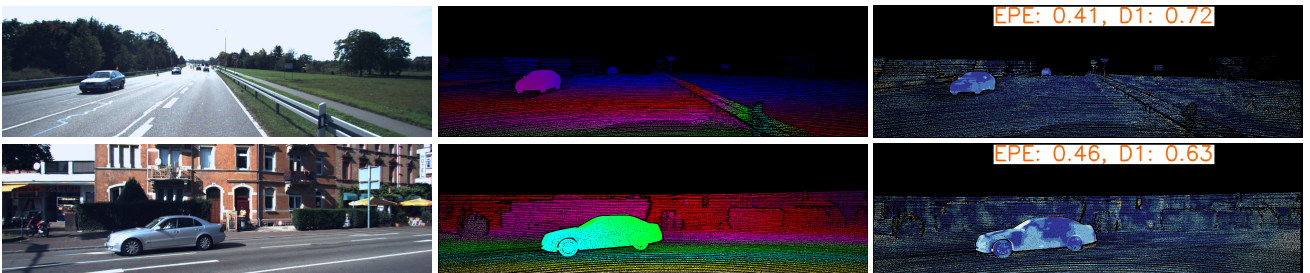


Figure 9. Disparity estimations and error maps embedded with error measures on the KITTI 2015 validation set. We finetuned TriStereoNet on KITTI 2015, assuming that the middle image is missed and the right one replaces it.

and multi-baseline pre-training and also self-supervision, which help the model to better learn the principles of stereo matching with more constraints coming from the setup. Figure 9 shows some qualitative results of the validation set.

## 4.2. Ablation Study

**Fusion Level and Fusion Method.** We first analyze the effect of the fusion level (location of the fusion) and also the method of fusion for combining the narrow- and wide-

baseline data. Table 3 shows the related results when models are only trained on the synthetic dataset. In all of these experiments, the models are trained with 30 epochs, and the best checkpoint is selected based on the least EPE on the test set.

In the cost level fusion, the proposed Guided Addition layer outperforms the other fusion techniques (except in EPE). We also analyzed average and simple addition in this level but discarded them as they are no better than the single

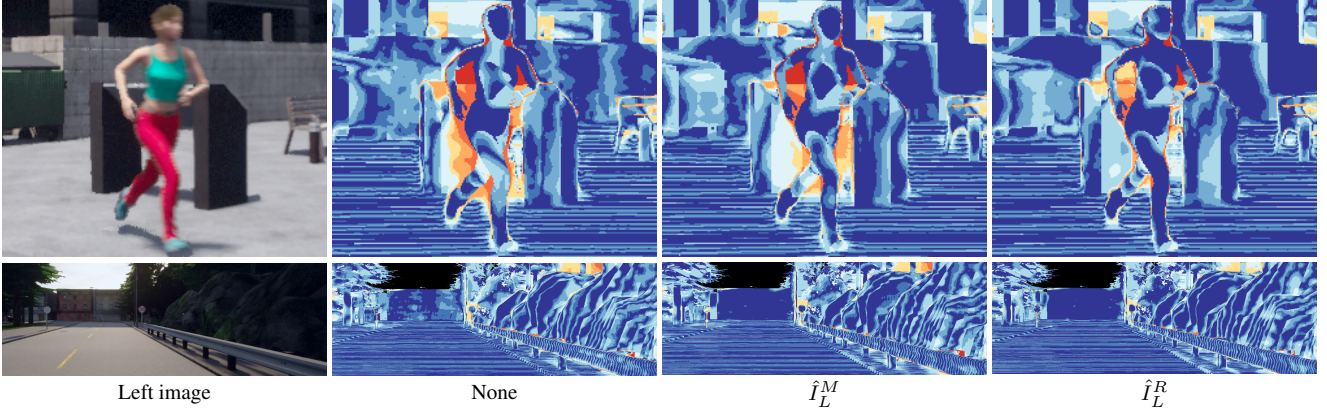


Figure 10. Qualitative comparison of disparity estimation error maps for self-supervised initialization with the real dataset. *2nd Column*: the model is trained from scratch on the synthetic dataset. *3rd & 4th Columns*: self-supervision with the real dataset is performed before supervised training on the synthetic dataset using the photometric losses of  $\hat{I}_L^M$  and  $\hat{I}_L^R$ , respectively.

wide baseline. This gain in performance increases when fusion is applied after the pre-hourglass and hourglass. Compared with average fusion, we see that not only the level of fusion is important, but the fusion method is similarly affecting the performance.

The  $hg_{avg}$  method shows more accurate results in terms of MRE and px-re-1 errors. We believe that this is because the hourglass module further processes two data streams. This regularization aggregates the disparity information regarding pixels’ locality, avoiding the many irrelevant spurious values in the final estimation. Nevertheless, we selected  $pre\_hg_{ga}$  for merging the data as it comes with less computational complexity than in  $hg_{avg}$ . Note that  $hg_{avg}$  requires the processing of two data flow (instead of one) in a heavy encoder-decoder with 3D convolutions.

**Trinocular vs. Binocular.** To prove the performance boost provided by the trinocular setup in comparison to the binocular case, we have exploited a similar network architecture for a single pair of images, *i.e.* either the left-middle or the left-right. Results are reported in Table 3. TriStereoNet, which fuses the two baseline streams, outperforms the single pairs in terms of all metrics.

**Learning Scheme.** Table 4 presents the impact of self-supervised initialization with the real dataset before training on the synthetic dataset in a supervised manner. It also compares the two methods by which we can reconstruct the reference image. It is clear that self-supervised initialization improves the results, particularly when  $\hat{I}_L^R$  is used for self-supervision. Figure 10 shows the qualitative comparison of these approaches. We also evaluated the case with summation of both the photometric losses of  $\hat{I}_L^M$  and  $\hat{I}_L^R$ , but it was not better than  $\hat{I}_L^R$  alone.

**Disparity Loss.** Last but not least, we evaluated the effect of the Huber loss for comparing disparity maps. Table 5 shows that Huber loss is outperforming smooth L1 loss for both binocular and trinocular settings. Note that Huber loss is equivalent to smooth L1 loss when  $\delta = 1$ . It also confirms

	Fusion	EPE(px)	D1(%)	px-1(%)	MRE	px-re-1(%)
LM	- - - -	0.63	2.65	8.87	0.062	0.76
LR	- - - -	0.54	2.33	7.05	0.057	0.71
LMR	- - - -	0.53	2.21	7.02	0.055	0.66
	$cost_{max}$	0.52	2.15	6.79	0.056	0.66
	$cost_{top}$	0.51	2.11	6.77	0.054	0.68
	$cost_{cat}$	0.53	2.07	6.60	0.053	0.61
	$cost_{ga}$	0.53	2.17	6.87	0.055	0.65
	$pre\_hg_{avg}$	<b>0.49</b>	<b>2.02</b>	6.39	0.052	0.64
	$pre\_hg_{ga}$	0.53	2.2	7.07	<b>0.051</b>	<b>0.58</b>
	$hg_{avg}$	<b>0.49</b>	<b>2.02</b>	<b>6.34</b>	0.054	0.65

Table 3. Comparison of the standard stereo with narrow (LM) and wide (LR) baselines (trained with binocular backbone adapted from GwcNet [12]) and the proposed trinocular stereo (LMR). Furthermore, different *levels* and *methods* of fusion are included. “ga” indicates the proposed Guided Addition fusion method.

$\hat{I}_L^M$ $\hat{I}_L^R$	EPE(px)	D1(%)	px-1(%)	MRE	px-re-1(%)
- - - -	0.49	2.02	6.39	0.052	0.64
✓ - - -	0.44	1.79	5.65	0.046	0.57
- ✓	<b>0.43</b>	<b>1.76</b>	<b>5.60</b>	<b>0.045</b>	<b>0.55</b>

Table 4. Effect of self-supervised initialization with the real dataset and different photometric losses using  $\hat{I}_L^M$  and  $\hat{I}_L^R$ . While in the first experiment, the model has been trained from scratch, the other two are trained after the self-supervised pre-training.

$\delta$	LM		LR		LMR	
	EPE(px)	MRE	EPE(px)	MRE	EPE(px)	MRE
1.00	0.68	0.067	0.58	0.061	0.54	0.057
0.75	0.64	0.065	0.57	0.059	0.53	0.057
0.50	0.66	0.065	0.56	0.058	0.51	0.056
0.25	<b>0.63</b>	<b>0.062</b>	<b>0.54</b>	<b>0.057</b>	<b>0.49</b>	<b>0.052</b>

Table 5. Effect of the  $\delta$  value in the Huber loss function. Huber loss with  $\delta = 1$  is equivalent to smooth L1 loss.

our choice of  $\delta$  as 0.25.

## 5. CONCLUSION

The paper proposed a deep end-to-end network for disparity estimation in a multi-baseline trinocular setup. The

pipeline processes two pairs of images from an axis-aligned three-camera configuration with narrow and wide baselines. We introduced a new layer for effectively merging the information of the two baselines. A synthetic dataset was generated to help with a proposed iterative sequential learning of real and synthetic datasets. With this learning mechanism, we can train on a real dataset with no ground-truth information. Experiments show that the proposed method outperforms the disparity map estimated by each image pair. This multi-baseline deep model is promising for building safe and reliable autonomous driving applications, where the image content is diversified and changeable in terms of the distance to the camera.

## References

- [1] Henrik Aanæs, Rasmus Ramsbøl Jensen, George Vogiatzis, Engin Tola, and Anders Bjarholm Dahl. Large-scale data for multiple-view stereopsis. *Int. J. Comput. Vis.*, 120(2):153–168, 2016. [2](#)
- [2] Konstantinos Batsos, Changjiang Cai, and Philippos Mordohai. CBMV: A coalesced bidirectional matching volume for disparity estimation. In *IEEE Conf. Comput. Vis. Pattern Recog.*, pages 2060–2069, 2018. [2](#)
- [3] Ivan Cabezas, Victor Padilla, and Maria Trujillo. BMPRE: An error measure for evaluating disparity maps. In *IEEE Int. Conf. on Sign. Process.*, volume 2, pages 1051–1055. IEEE, 2012. [5](#)
- [4] Jia-Ren Chang and Yong-Sheng Chen. Pyramid stereo matching network. In *IEEE Conf. Comput. Vis. Pattern Recog.*, pages 5410–5418, 2018. [1](#), [2](#), [3](#), [4](#), [6](#)
- [5] Yong-Sheng Chen, Yi-Ping Hung, and Chiou-Shann Fuh. Fast block matching algorithm based on the winner-update strategy. *IEEE Trans. Image Process.*, 10(8):1212–1222, 2001. [2](#)
- [6] Alexey Dosovitskiy, German Ros, Felipe Codevilla, Antonio Lopez, and Vladlen Koltun. CARLA: An open urban driving simulator. *arXiv preprint arXiv:1711.03938*, 2017. [5](#)
- [7] Shivam Duggal, Shenlong Wang, Wei-Chiu Ma, Rui Hu, and Raquel Urtasun. Deeprunner: Learning efficient stereo matching via differentiable patchmatch. In *IEEE Conf. Comput. Vis. Pattern Recog.*, pages 4384–4393, 2019. [4](#)
- [8] Yasutaka Furukawa and Carlos Hernández. Multi-view stereo: A tutorial. *Foundations and Trends in Computer Graphics and Vision*, 9(1-2):1–148, 2015. [2](#)
- [9] David Gallup, Jan-Michael Frahm, Philippos Mordohai, and Marc Pollefeys. Variable baseline/resolution stereo. In *IEEE Conf. Comput. Vis. Pattern Recog.*, pages 1–8. IEEE, 2008. [2](#), [3](#)
- [10] Stefan K Gehrig and Uwe Franke. Improving stereo sub-pixel accuracy for long range stereo. In *Int. Conf. Comput. Vis.*, pages 1–7. IEEE, 2007. [2](#)
- [11] Clément Godard, Oisín Mac Aodha, and Gabriel J Brostow. Unsupervised monocular depth estimation with left-right consistency. In *IEEE Conf. Comput. Vis. Pattern Recog.*, pages 270–279, 2017. [4](#)
- [12] Xiaoyang Guo, Kai Yang, Wukui Yang, Xiaogang Wang, and Hongsheng Li. Group-wise correlation stereo network. In *IEEE Conf. Comput. Vis. Pattern Recog.*, pages 3273–3282, 2019. [1](#), [2](#), [3](#), [4](#), [6](#), [8](#)
- [13] Philipp Heise, Sebastian Klose, Brian Jensen, and Alois Knoll. Pm-huber: Patchmatch with huber regularization for stereo matching. In *Int. Conf. Comput. Vis.*, pages 2360–2367, 2013. [4](#)
- [14] Simon Hermann, Sandino Morales, and Reinhard Klette. Half-resolution semi-global stereo match. In *IEEE Intelligent Vehicles Symposium (IV)*, pages 201–206, July 2011. [5](#)
- [15] Heiko Hirschmüller. Accurate and efficient stereo processing by semi-global matching and mutual information. In *IEEE Conf. Comput. Vis. Pattern Recog.*, volume 2, pages 807–814. IEEE, 2005. [1](#), [2](#)
- [16] Dominik Honegger, Torsten Sattler, and Marc Pollefeys. Embedded real-time multi-baseline stereo. In *IEEE Int. Conf. on Robotics and Automation (ICRA)*, pages 5245–5250. IEEE, 2017. [2](#), [3](#)
- [17] Jan Kallwies, Torsten Engler, Bianca Forkel, and Hans-Joachim Wuensche. Triple-SGM: Stereo processing using semi-global matching with cost fusion. In *IEEE Conf. on App. of Comput. Vis.*, pages 192–200, 2020. [2](#), [3](#)
- [18] Jan Kallwies and Hans-Joachim Wuensche. Effective combination of vertical and horizontal stereo vision. In *IEEE Conf. on App. of Comput. Vis.*, pages 1992–2000. IEEE, 2018. [2](#), [3](#)
- [19] Alex Kendall, Hayk Martirosyan, Saumitro Dasgupta, Peter Henry, Ryan Kennedy, Abraham Bachrach, and Adam Bry. End-to-end learning of geometry and context for deep stereo regression. In *Int. Conf. Comput. Vis.*, pages 66–75, 2017. [1](#), [2](#), [4](#)
- [20] Diederik P Kingma and Jimmy Ba. Adam: A method for stochastic optimization. *arXiv preprint arXiv:1412.6980*, 2014. [6](#)
- [21] Nikolaus Mayer, Eddy Ilg, Philip Hausser, Philipp Fischer, Daniel Cremers, Alexey Dosovitskiy, and Thomas Brox. A large dataset to train convolutional networks for disparity, optical flow, and scene flow estimation. In *IEEE Conf. Comput. Vis. Pattern Recog.*, pages 4040–4048, 2016. [2](#)
- [22] Sky McKinley and Megan Levine. Cubic spline interpolation. *College of the Redwoods*, 45(1):1049–1060, 1998. [3](#)
- [23] Moritz Menze and Andreas Geiger. Object scene flow for autonomous vehicles. In *IEEE Conf. Comput. Vis. Pattern Recog.*, pages 3061–3070, 2015. [6](#)
- [24] Matthias Michael, Jan Salmen, Johannes Stallkamp, and Marc Schlipsing. Real-time stereo vision: Optimizing semi-global matching. In *IEEE Intelligent Vehicles Symposium (IV)*, pages 1197–1202. IEEE, 2013. [2](#)
- [25] Karsten Mühlmann, Dennis Maier, Jürgen Hesser, and Reinhard Männer. Calculating dense disparity maps from color stereo images, an efficient implementation. *Int. J. Comput. Vis.*, 47(1-3):79–88, 2002. [2](#)
- [26] Masatoshi Okutomi and Takeo Kanade. A multiple-baseline stereo. *IEEE Trans. Pattern Anal. Mach. Intell.*, 15(4):353–363, 1993. [3](#)
- [27] Konstantin Schauwecker, Sandino Morales, Simon Hermann, and Reinhard Klette. A comparative study of stereo-matching algorithms for road-modeling in the presence of windscreen wipers. In *IEEE Intelligent Vehicles Symposium (IV)*, pages 7–12, June 2011. [5](#)

- [28] Akihito Seki and Marc Pollefeys. SGM-Nets: Semi-global matching with neural networks. In *IEEE Conf. Comput. Vis. Pattern Recog.*, pages 231–240, 2017. 1, 2
- [29] Faranak Shamsafar, Samuel Woerz, Rafia Rahim, and Andreas Zell. MobileStereoNet: Towards lightweight deep networks for stereo matching. *arXiv preprint arXiv:2108.09770*, 2021. 2
- [30] Zhelun Shen, Yuchao Dai, and Zhibo Rao. CFNet: Cascade and fused cost volume for robust stereo matching. In *IEEE Conf. Comput. Vis. Pattern Recog.*, pages 13906–13915, 2021. 4
- [31] Wannes Van Der Mark and Darius M Gavrilă. Real-time dense stereo for intelligent vehicles. *IEEE Trans. on Intelligent Transportation Systems*, 7(1):38–50, 2006. 5
- [32] Zhou Wang, Alan C Bovik, Hamid R Sheikh, and Eero P Simoncelli. Image quality assessment: from error visibility to structural similarity. *IEEE Trans. Image Process.*, 13(4):600–612, 2004. 4
- [33] Jiabin Xing, Zhi Qi, Jiying Dong, Jiaxuan Cai, and Hao Liu. MABNet: A lightweight stereo network based on multi-branch adjustable bottleneck module. In *Eur. Conf. Comput. Vis.*, pages 340–356. Springer, 2020.
- [34] Bin Xu, Yuhua Xu, Xiaoli Yang, Wei Jia, and Yulan Guo. Bilateral grid learning for stereo matching networks. In *IEEE Conf. Comput. Vis. Pattern Recog.*, pages 12497–12506, 2021.
- [35] Haofei Xu and Juyong Zhang. AANet: Adaptive aggregation network for efficient stereo matching. In *IEEE Conf. Comput. Vis. Pattern Recog.*, pages 1959–1968, 2020.
- [36] Ramin Zabih and John Woodfill. Non-parametric local transforms for computing visual correspondence. In *Eur. Conf. Comput. Vis.*, pages 151–158. Springer, 1994. 1
- [37] Jure Žbontar and Yann LeCun. Stereo matching by training a convolutional neural network to compare image patches. *Journal of Machine Learning Research*, 17(1):2287–2318, 2016. 1, 2
- [38] Jure Žbontar, Yann LeCun, et al. Stereo matching by training a convolutional neural network to compare image patches. *J. Mach. Learn. Res.*, 17(1):2287–2318, 2016.
- [39] Feihu Zhang, Victor Prisacariu, Ruigang Yang, and Philip HS Torr. GA-Net: Guided aggregation net for end-to-end stereo matching. In *IEEE Conf. Comput. Vis. Pattern Recog.*, pages 185–194, 2019. 1, 2, 4, 6

## TriStereoNet: A Trinocular Framework for Multi-baseline Disparity Estimation (Appendix)

The results on the KITTI 2015 benchmark (200 test images) are reported in Table. 1. We see that in the binocular deployment of TriStereoNet, this model is still capable of estimating the disparity with superior or competitive accuracy to the inherent binocular models.

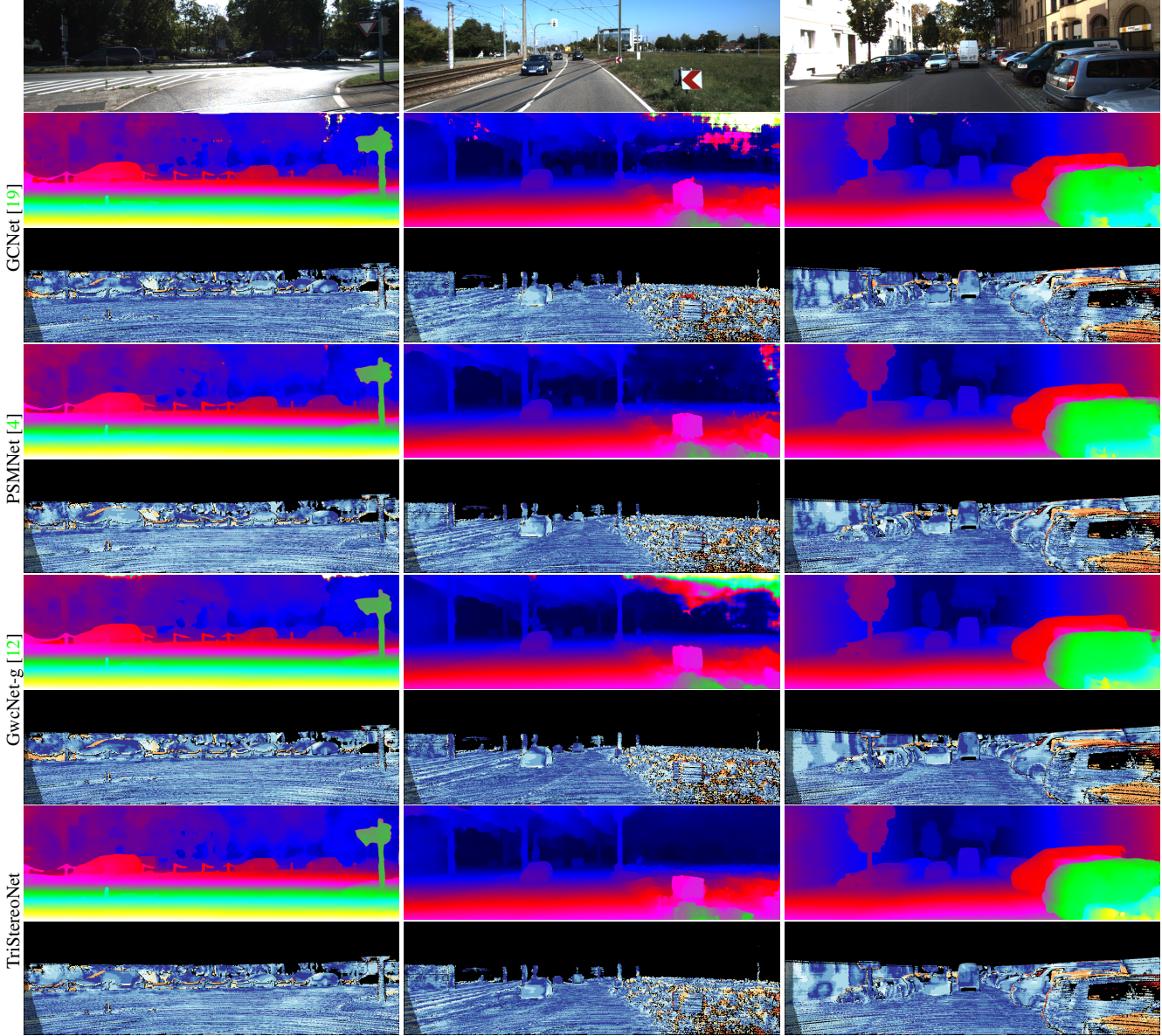


Figure 1. Qualitative performance (disparity images together with error maps) on KITTI 2015 benchmark. We assume TriStereoNet is missing the viewpoint of the middle camera for this binocular dataset.

Fig. 1 illustrates some qualitative results. By visual inspection, we noticed that TriStereoNet performs more robust in difficult areas, *i.e.* in rich-textured and detailed segments (*e.g.* trees), distant objects/regions (*e.g.* distant cars, trees or sky), and challenging illuminated areas (*e.g.* very bright regions). Note that almost the upper half of the KITTI images do not have the ground-truth annotations of LiDAR. This causes other models to estimate inaccurate or erroneous disparity values in these regions as they cannot learn due to a lack of supervision for related areas. The upper half of the images includes contents

such as trees, buildings, street-covered areas, or the sky. For instance, some sky-related parts are wrongly estimated by other approaches with very high disparity values (very close range). However, TriStereoNet performs with great superiority in these regions thanks to its self-supervised pre-training with three cameras.

Methods	All(%)			Noc(%)		
	$D1_{bg}$	$D1_{fg}$	$D1_{all}$	$D1_{bg}$	$D1_{fg}$	$D1_{all}$
MC-CNN [38]	2.89	8.88	3.89	2.48	7.64	3.33
GCNet [19]	2.21	6.16	2.87	2.02	5.58	2.61
AANet [35]	1.99	5.39	2.55	1.80	4.93	2.32
BGNet [34]	2.07	4.74	2.51	1.91	4.34	2.31
MABNet [33]	1.89	5.02	2.41	1.74	4.59	2.21
TriStereoNet	1.86	4.77	2.35	1.68	4.12	2.09
PSMNet [4]	1.86	4.62	2.32	1.71	4.31	2.14
DeepPruner [7]	1.87	3.56	2.15	1.71	3.18	1.95
GwcNet-g [12]	1.74	3.93	2.11	1.61	3.49	1.92

Table 1. Evaluation results on the KITTI 2015 benchmark with D1 measure for non-occluded and all pixels in background, foreground and all areas. The models are sorted according to  $D1_{all}$ ; the lower, the better.